Journal Pre-proof

High-pressure synthesis and high-performance half metallicity of quadruple perovskite oxide $DyCu_3Fe_2Re_2O_{12}$

Zhehong Liu , Jinfeng Peng , Xiao Wang , Fedor Temnikov , Alexey Ushakov , Xubin Ye , Zhao Pan , Jie Zhang , Maocai Pi , Shuai Tang , Kai Chen , Florin Radu , Zhiwei Hu , Chien-Te Chen , Zhenhua Chi , Zlata Pchelkina , Valentin Irkhin , Yao Shen , Sergey V. Streltsov , Youwen Long

PII: S2667-3258(24)00515-6
DOI: https://doi.org/10.1016/j.fmre.2024.11.024
Reference: FMRE 928

To appear in: *Fundamental Research*

Received date: 24 September 2024
Revised date: 17 November 2024
Accepted date: 27 November 2024

Please cite this article as: Zhehong Liu , Jinfeng Peng , Xiao Wang , Fedor Temnikov , Alexey Ushakov , Xubin Ye , Zhao Pan , Jie Zhang , Maocai Pi , Shuai Tang , Kai Chen , Florin Radu , Zhiwei Hu , Chien-Te Chen , Zhenhua Chi , Zlata Pchelkina , Valentin Irkhin , Yao Shen , Sergey V. Streltsov , Youwen Long , High-pressure synthesis and high-performance half metallicity of quadruple perovskite oxide $DyCu_3Fe_2Re_2O_{12}$, *Fundamental Research* (2024), doi: https://doi.org/10.1016/j.fmre.2024.11.024

High-pressure synthesis and high-performance half metallicity of quadruple perovskite oxide $DyCu_3Fe_2Re_2O_{12}$

Zhehong Liu[a,b,†], Jinfeng Peng[a,†], Xiao Wang[a], Fedor Temnikov[c], Alexey Ushakov[c], Xubin Ye[a,b], Zhao Pan[a,b], Jie Zhang[a,b], Maocai Pi[a,b], Shuai Tang[a,b], Kai Chen[d], Florin Radu[e], Zhiwei Hu[f], Chien-Te Chen[g], Zhenhua Chi[h], Zlata Pchelkina[c], Valentin Irkhin[c], Yao Shen[a,b], Sergey V. Streltsov[c,i,] *, Youwen Long[a,b,j,]*

[a]Beijing National Laboratory for Condensed Matter Physics, Institute of Physics, Chinese Academy of Sciences, Beijing 100190, China

[b]School of Physical Sciences, University of Chinese Academy of Sciences, Beijing 100049, China

[c]Institute of Metal Physics, Russian Academy of Sciences, Yekaterinburg, 620108 Russia

[d]National Synchrotron Radiation Laboratory, University of Science and Technology of China, Hefei 230026, China

[e]Helmholtz-Zentrum Berlin fur Materialien und Energie, Albert-Einstein-Str.15, 12489 Berlin, Germany

[f]Max Planck Institute for Chemical Physics of Solids, Nöthnitzer Straße 40, 01187 Dresden, Germany

[g]National Synchrotron Radiation Research Center (NSRRC), Hsinchu Science Park, Hsinchu 300092, Taiwan

[h]Institute of Plasma Physics, HFIPS, Chinese Academy of Sciences, Hefei, 230031, China

[i]Department of Theoretical Physics and Applied Mathematics, Ural Federal University, Mira St. 19, 620002 Ekaterinburg, Russia

[j]Songshan Lake Materials Laboratory, Dongguan, Guangdong 523808, China

*Corresponding emails: streltsov.s@gmail.com; ywlong@iphy.ac.cn

[†]Equally contributed to this work.

ABSTRACT

The *A*- and *B*-site ordered quadruple perovskite oxide $DyCu_3Fe_2Re_2O_{12}$ with cubic *Pn*-3 symmetry was synthesized under high-pressure and high-temperature conditions. The material experiences a sharp long-range ferrimagnetic transition arising from the strong superexchange antiferromagnetic interactions of Cu-Re and Fe-Re at a high Curie temperature ($T_C \approx 660$ K). Owing to the influence at lower temperatures of the antiferromagnetic ordering of the Dy^{3+} occupying the *A*-site, the susceptibility of $DyCu_3Fe_2Re_2O_{12}$ decreases continuously below 50 K, which is essentially different from that of the isostructural compound $LaCu_3Fe_2Re_2O_{12}$. Moreover, in the presence of a magnetic field, the *A*-site Dy^{3+} spins are readily transformed into the ferromagnetic state from the antiferromagnetic ground state. Thus, the saturated magnetic moment of $DyCu_3Fe_2Re_2O_{12}$ is sharply enhanced from 7.0 μ_B/f.u. at 300 K to 14 μ_B/f.u. at 2 K by applying a magnetic field of 7 T. Theoretical calculations suggest that $DyCu_3Fe_2Re_2O_{12}$ is a half-metallic ferrimagnet with a spin-up band gap of approximately 2.0 eV. The combination of the high Curie temperature, wide half-metallic energy gap, and large magnetic moment makes $DyCu_3Fe_2Re_2O_{12}$ promising for potential applications in advanced spintronic devices.

1. Introduction

A magnetic half metal (HM) is a type of material that behaves as a conductor for electrons of a particular spin orientation, whereas it becomes an insulator or semiconductor for electrons with the opposite spin projection [1-3]. This unique property arises from the band structure of the HM, where the electronic density of states at the Fermi level is metallic in one spin direction and gapped in the other. As a result, in principle, the carriers of HMs exhibit 100% spin polarization, which renders the material highly valuable for spintronic applications in which the spin of electrons, rather than their charge, is utilized to transmit and store information. This unique electronic structure, together with the potential for applications in high-efficiency spintronic devices, have resulted in HMs being extensively researched in the fields of

materials science and condensed matter physics [1-4].

To date, many types of half-metallic materials, including the oxides CrO_2 and Fe_3O_4, Heusler alloys NiMnSb [1,5-7], and perovskites Sr_2FeMoO_6 [4], $LaCu_3Fe_2Re_2O_{12}$ [8], and $La_{1-x}Sr_xMnO_3$ [9], have been discovered by theoretical calculations or experiments (see also [3]). Among them, *A*- and *B*-site ordered quadruple perovskites with the formula $AA'_3B_2B'_2O_{12}$ often have exceptional properties, such as a high Curie temperature, large saturated moment, and wide band gap [8,10-12]. The Curie temperature of materials in this family can be markedly enhanced by inserting the magnetic ion Cu^{2+} at the *A*′-site [12,13] as an effective approach to optimize the magnetic properties. Furthermore, the additional magnetic interactions that arise as a result of the occupation of the *A*-site by a magnetic ion can either enhance or compete with those arising from the magnetic ions at the *A*-, *B*-, and *B*′-site. These interactions include both direct and super-exchange interactions mediated by oxygen ions. Therefore, manipulation of the interactions between the ions at the *A*- and *B*-site enables magnetic properties, such as the Curie temperature, magnetization moment, and spin alignment, to be tailored to develop advanced materials, thereby opening new possibilities for innovations in electronics, data storage, and spin-based technologies. To date, the influence of *A*-site magnetic lanthanide ions in *A*-site ordered quadruple perovskites, such as $LnCu_3Mn_4O_{12}$ (*Ln* = magnetic lanthanide ions) family, has been studied in detail [14,15]. However, detailed experimental studies have not yet been conducted to clarify the influence of magnetic ions at the *A*-site of *A*- and *B*-site quadruple perovskites. In our study, an all-magnetic-cation *A*- and *B*-site quadruple perovskite $DyCu_3Fe_2Re_2O_{12}$ (DCFRO) with excellent half-metallic properties was prepared by high-pressure and high-temperature methods. The unusual magnetic behavior of this material differs considerably from those of its isostructural counterparts.

2. Experimental and calculation methods

2.1. Sample preparation.

Polycrystalline $DyCu_3Fe_2Re_2O_{12}$ was synthesized by combining high purity (≥ 99.9%) dysprosium oxide (Dy_2O_3), copper oxide (CuO), iron (III) oxide (Fe_2O_3), rhenium (Re), and rhenium (VII) oxide (Re_2O_7) in the mole ratio 7:42:14:10:9. After thoroughly grinding the starting material in an agate mortar, the mixture was pressed into a gold capsule and subjected to 9 GPa and 1223 K for half an hour using a cubic-anvil-type high-pressure apparatus. Finally, the products were quickly quenched to room temperature and the pressure was slowly released.

2.2. X-ray powder diffraction.

Room-temperature (RT) X-ray diffraction (XRD) was performed using a Huber diffractometer with Cu $K_{\alpha 1}$. The XRD data were analyzed using the Rietveld refinement program GSAS [16].

2.3. X-ray absorption spectroscopy and magnetic circular dichroism.

The RT X-ray absorption spectra (XAS) at the Cu-$L_{2,3}$ and Fe-$L_{2,3}$ edges were measured on the BL11A beamline of the NSRRC synchrotron in total electron yield (TEY) mode, whereas the Re-L_3 XAS was measured on the TLS08A beamline of the NSRRC in transmission mode. The X-ray magnetic circular dichroism (XMCD) spectra at the Cu-$L_{2,3}$ and Fe-$L_{2,3}$ edges were collected at 8 K and 6 T at the VEKMAG end station [17] of the HZB/BESSY II/Germany Synchrotron Radiation Facility. The XMCD spectra at the Dy-$M_{4,5}$ edges were collected at 8 K under a 6 T magnetic field and at 20 K, 100 K, and 300 K by applying a 0.01 T magnetic field at the VEKMAG endstation. All XMCD spectra were acquired in the TEY mode, with a fresh surface prepared by cleaving the sample *in situ* under ultrahigh vacuum (10^{-10} mbar) a few minutes before the measurements were conducted.

2.4. Magnetic, electrical, and thermal properties measurements.

The magnetic susceptibility and isothermal magnetization were measured using a commercial superconducting quantum interference device (SQUID) magnetometer (Quantum Design, MPMS-7 T). The magnetic susceptibility was collected in both zero-field-cooled (ZFC) and field-cooled (FC) modes with a field of 0.1 T across a temperature range of 2–800 K. The isothermal magnetization as a function of the

magnetic field was measured at selected temperatures (2, 20, 50, 100, 300, 500 and 750 K) within a range of −7 to 7 T. The electrical transport properties were measured using a standard four-probe method on a physical property measurement system (Quantum Design, PPMS-9 T) from 2 to 300 K. The field dependence of the isothermal magnetoresistance was acquired from −7 to 7 T at 2, 50, and 150 K. Specific heat (C_p) measurements were carried out using a pulse relaxation method on the PPMS by varying the temperature from 2 to 100 K at 0 T and from 2 to 22 K at 0.1, 0.3, 1.0, and 3 T.

2.5. Electronic structure calculation.

We used the generalized gradient approximation (GGA) [18], which was corrected to consider strong electronic correlations via the GGA+U method [19] and the spin-orbit coupling. We chose the following interaction parameters $(U\text{-}J_H)^{Dy} = 7$ eV, $(U\text{-}J_H)^{Cu} = 7$ eV, $(U\text{-}J_H)^{Fe} = 4.1$ eV, $(U\text{-}J_H)^{Re} = 1.5$ eV. These values are not only typical and widely used in the literature [20], but, more importantly, the half-metallic ground state does not depend on the particular values assigned to these parameters (within reasonable limits), as discussed in Sec. 3. Brillouin-zone integration was performed using 125 k-points. All the calculations were performed using the VASP program code [21] and the projector augmented-wave method [22]. The cut-off energy was set to 500 eV. Classical Monte Carlo simulations were performed using the *spinmc* algorithm in the ALPS package [23].

3. Results and discussion

3.1. X-ray powder diffraction and crystal structure

Figure 1a shows the XRD pattern (measured at RT) and Rietveld refinement results for DCFRO. All the diffraction peaks are well fitted based on an $AA'_3B_2B'_2O_{12}$-type *A*-site and *B*-site ordered quadruple perovskite structure model with cubic symmetry (*Pn*-3 space group), resulting in a lattice constant of $a = 7.44611(1)$ Å. The presence of sharp diffraction peaks with Miller indices h + k + l = odd, such as (111), (311), (331), and (333), provide strong evidence for rocksalt-type ordering

between Fe at the *B*-site and Re at the *B*'-site. Because of the significant difference in the X-ray scattering factors of Fe and Re, the degree of order between these two atoms can be determined by fitting the occupancy parameter. In our refinement, the occupancy factors for both Fe and Re were found to be nearly 100%, indicating negligible Fe-Re antisite disorder. Therefore, the occupancy factors of Fe and Re were set to unity as the basis on which to refine the other structural parameters, which resulted in reasonable structural parameters and satisfactory goodness-of-fit values. The detailed refinement parameters are listed in Supplementary **Table S1**.

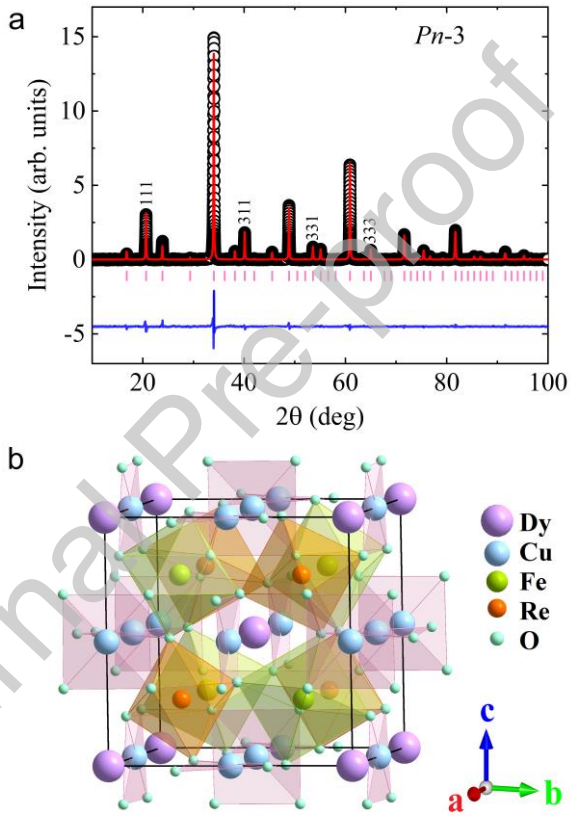

Fig. 1. (a) XRD pattern and refined results of DCFRO with cubic *Pn*-3 symmetry at room temperature. The observed (black circles), calculated (red solid line) and difference (blue solid line) are shown. The magenta ticks indicate the permitted Bragg reflections for the space group *P*n-3. (b) Schematic crystal structure diagram of *A*- and *B*-site ordered quadruple perovskite DCFRO. Atomic sites: Dy 2*a* (0.25, 0.25, 0.25), Cu 6*d* (0.25, 0.75, 0.75), Fe 4*b* (0, 0, 0), Re 4*c* (0.5, 0.5, 0.5), and O 24*g* (*x*, *y*, *z*). The CuO_4 square plaquettes and corner-shared Fe/ReO_6 octahedra are shown.

Fig. 1b shows a schematic diagram of the DCFRO crystal structure. Unlike the twelve-fold coordinated Dy atoms occupying the *A*-site, the Cu atoms at the *A*'-site form square-planar CuO_4 units because of their significantly smaller ionic radii and

strong Jahn-Teller effects. These spatially isolated CuO_4 units are connected to the *B*/*B*′-site FeO_6/ReO_6 octahedra by sharing oxygen atoms. Bond valence sum (BVS) analysis was used to determine the valence states of Cu and Fe as +2 and +3, respectively (**Tab. S1**). Refinement of the Re-O bond length in DCFRO yielded the value of 1.947 Å, which is close to that observed for $LaCu_3Fe_2Re^{4.5+}{}_2O_{12}$ (1.960 Å) [8], suggesting that the valence state of Re in DCFRO is approximately +4.5 on average.

3.2. Valence state of magnetic ions

XAS is a sensitive technique for determining the valence states and local environments of transition metals (TMs). **Fig. 2**a and b display the XAS results at the Cu- and Fe-$L_{2,3}$ edges of DCFRO, along with those of $CaCu_3Ti_4O_{12}$ (CCTO) as a Cu^{2+} reference [24] and $LaCu_3Fe_2Re_2O_{12}$ (LCFRO) as an Fe^{3+} reference, both of which have similar coordination environments to that of DCFRO [8]. The DCFRO spectra at the Cu- and Fe-$L_{2,3}$ edges closely resemble the shapes and energies of the peaks of the Cu^{2+} and Fe^{3+} references [8,24], respectively, thereby confirming the presence of Cu^{2+} and Fe^{3+} in DCFRO. **Fig. 2c** shows the Re-L_3 edge of DCFRO, along with those of LCFRO and $CaCu_3Co_2Re_2O_{12}$ (CCCRO) as $Re^{4.5+}$ and Re^{6+} references [8,25], respectively. The energy of the Re-L_3 edge for DCFRO is almost the same as that of the $Re^{4.5+}$ reference and is shifted to a lower energy by approximately 1.5 eV relative to that of the Re^{6+} reference. This suggests that Re has a valence state of +4.5 in DCFRO, which aligns with the charge balance requirement. Furthermore, in *A*-site ordered quadruple perovskites, the valence state of Dy at the *A*-site tends to be +3 [26]. By combining the results of the XAS and bond valence sum (BVS) analyses, we can safely conclude that the charge configuration of DCFRO is $DyCu^{2+}{}_3Fe^{3+}{}_2Re^{4.5+}{}_2O_{12}$.

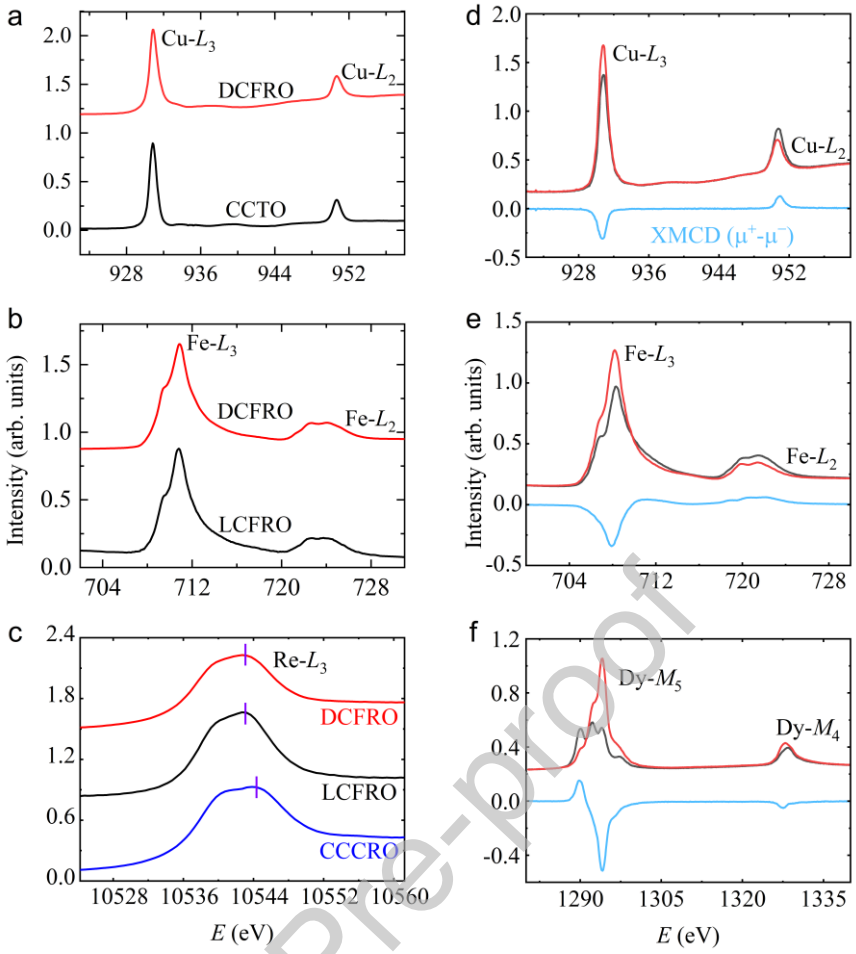

Fig. 2. XAS at the (a) Cu-$L_{2,3}$, (b) Fe-$L_{2,3}$ and (c) Re-L_3 edges of DCFRO measured at room temperature. CCTO, LCFRO and CCFRO are shown as references for comparison. The vertical purple lines in (c) indicate the peak positions of the Re-L_3 XAS. XMCD at (d) Cu-$L_{2,3}$, (e) Fe-$L_{2,3}$ and (f) Dy-$M_{4,5}$ edges of DCFRO measured at 8 K and 6 T. The photon spin aligning parallel (μ^+ black lines) and antiparallel (μ^- red lines) to the applied magnetic field are shown in black and red lines, respectively. The difference spectra XMCD (μ^+-μ^-) are shown in light blue.

3.3. Magnetic properties

Fig. 3a shows the temperature dependence of the magnetic susceptibility (χ) below 750 K during exposure to a magnetic field of 0.1 T in the ZFC and FC modes. The sharp increase in the susceptibility as the temperature decreases to $T_C \approx 660$ K indicates the occurrence of a ferromagnetic (FM) or ferrimagnetic (FiM) phase transition. Unlike the single FiM transition observed for the isostructural material LCFRO, where the susceptibility tends to saturate below T_C, the susceptibility of DCFRO exhibits a dome near 50 K, below which the susceptibility decreases rapidly. This behavior suggests that the Dy^{3+} occupying the *A*-site may start to take on antiferromagnetic (AFM) ordering below approximately 50 K while being exposed to

the weak magnetic field of 0.1 T.

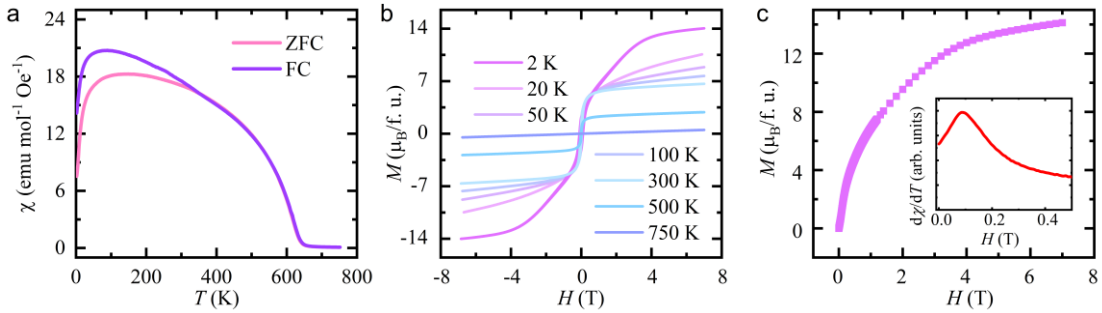

Fig. 3. (a) Temperature dependence of magnetic susceptibility measured at 0.1 T with ZFC and FC mode. (b) Field dependence of magnetization measured at some selected temperatures. (c) Field dependence of initial magnetization measured at 2 K. The inset shows the field-dependent derivative of the initial magnetization at low magnetic field.

The field dependence of the magnetization behavior provides more evidence of the FM or FiM long-range order in DCFRO. As shown in **Fig. 3**b, the magnetization varies linearly with the field above T_C (e.g., at 750 K), which is consistent with the paramagnetism observed in magnetic susceptibility. However, below T_C, typical magnetic hysteresis features are observed. The saturated moment observed at 300 K is approximately 7.0 μ_B/f.u., which further increases to 14.0 μ_B/f.u. at 2 K. **Fig. 3**c shows the dependence on the magnetic field of the initial magnetization measured at 2 K. In weak magnetic fields ($\leq$ 0.1 T), the magnetization increases rapidly, likely driven primarily by the combination of FiM ordering $Cu^{2+}(\uparrow)$-$Fe^{3+}(\uparrow)$-$Re^{4.5+}(\downarrow)$, similar to that observed for the isostructural compounds $Ca/LaCu_3Fe_2Re_2O_{12}$ [8,10] and collinear AFM contributed by Dy^{3+}. At 0.1 T, the magnetic order of Dy^{3+} is expected from collinear AFM to non-collinear magnetic order. As the field strength continues to increase, the magnetization initially grows almost linearly, after which its slope gradually decreases and the spin order of Dy^{3+} probably changes from non-collinear magnetic order to collinear FM near 4.0 T. Eventually, it may achieve saturation magnetization values at fields stronger than 7.0 T. This indicates that magnetic ions at the *A*-site (Dy^{3+}) gradually align such that they are arranged parallel to each other as the magnetic field strengthens. The inset of **Fig. 3**c shows the field-dependence derivative of the initial magnetization; the well-defined peak that appears at approximately 0.1 T may be a signature of the metamagnetic transition of

Dy^{3+} from the collinear AFM to the non-collinear magnetic order. Because four different magnetic ions occupy different sites in DCFRO, eight different collinear spin alignments, i.e., the FM $Dy^{3+}(\uparrow)Cu^{2+}(\uparrow)$-$Fe^{3+}(\uparrow)$-$Re^{4.5+}(\uparrow)$, FiM $Dy^{3+}(\uparrow)Cu^{2+}(\uparrow)$-$Fe^{3+}(\uparrow)$-$Re^{4.5+}(\downarrow)$, $Dy^{3+}(\uparrow)Cu^{2+}(\uparrow)$-$Fe^{3+}(\downarrow)$-$Re^{4.5+}(\uparrow)$, $Dy^{3+}(\uparrow)Cu^{2+}(\downarrow)$-$Fe^{3+}(\uparrow)$-$Re^{4.5+}(\uparrow)$, $Dy^{3+}(\downarrow)Cu^{2+}(\uparrow)$-$Fe^{3+}(\uparrow)$-$Re^{4.5+}(\downarrow)$, $Dy^{3+}(\downarrow)Cu^{2+}(\uparrow)$-$Fe^{3+}(\downarrow)$-$Re^{4.5+}(\uparrow)$, and $Dy^{3+}(\downarrow)Cu^{2+}(\downarrow)$-$Fe^{3+}(\uparrow)$-$Re^{4.5+}(\uparrow)$ could possibly occur as the magnetic ground state. If we only consider the spin contribution for Dy^{3+}, Cu^{2+}, Fe^{3+}, and $Re^{4.5+}$, the corresponding saturated moments for the eight spin alignments are 23.0, 13.0, 3.0, 17.0, 13.0, 3.0, 7.0 and 7.0 μ_B/f.u., respectively. Based on the saturated moments measured at 2 K and 7 T (14.0 μ_B/f.u.), the $Dy^{3+}(\uparrow)Cu^{2+}(\uparrow)$-$Fe^{3+}(\uparrow)$-$Re^{4.5+}(\downarrow)$, and $Dy^{3+}(\downarrow)Cu^{2+}(\uparrow)$-$Fe^{3+}(\uparrow)$-$Re^{4.5+}(\uparrow)$ FiM orders (13.0 μ_B/f.u.) appear to be the most likely. Furthermore, considering the strong spin-orbit coupling in Dy^{3+} and $Re^{4.5+}$, Dy^{3+} would have a saturated magnetic moment larger than 5.0 μ_B, whereas that of $Re^{4.5+}$ would be smaller than 2.5 μ_B and thus the spin alignment $Dy^{3+}(\uparrow)Cu^{2+}(\uparrow)$-$Fe^{3+}(\uparrow)$-$Re^{4.5+}(\downarrow)$ is more rational than $Dy^{3+}(\downarrow)Cu^{2+}(\uparrow)$-$Fe^{3+}(\uparrow)$-$Re^{4.5+}(\uparrow)$ in a strong magnetic field and at low temperatures. This conclusion agrees with the results of the total-energy GGA+U+SOC calculations presented in the next section. In contrast, the saturation moment of DCFRO measured at 300 K was close to 7.0 μ_B/f.u., which is similar to that observed for the isostructural compound $LaCu_3Fe_2Re_2O_{12}$[8] with a spin alignment of $Cu^{2+}(\uparrow)$-$Fe^{3+}(\uparrow)$-$Re^{4.5+}(\downarrow)$. Therefore, the FiM $Dy^{3+}(\uparrow)Cu^{2+}(\uparrow)$–$Fe^{3+}(\uparrow)$–$Re^{4.5+}(\downarrow)$ spin coupling most probably occurs in DCFRO in the presence of a strong magnetic field.

3.4. Spin alignment of magnetic ions

To further clarify the spin alignment of DCFRO, element-selective XMCD measurements in a field of 6 T were conducted at the $L_{2,3}$ edges of Cu and Fe and the $M_{2,3}$ edges of Re. As shown in **Fig. 2**d-f, the L_3 (L_2) edges and M_5 (M_4) were all negative (positive) for Cu, Fe, and Dy, indicative of FM $Dy^{3+}(\uparrow)Cu^{2+}(\uparrow)Fe^{3+}(\uparrow)$ ordering in a strong magnetic field. Considering the strong superexchange AFM

coupling of Fe-Re/Os and formation of robust FiM Cu(↑)-Fe(↑)-Re/Os(↓) ordering in the isostructural *A*- and *B*-site ordered quadruple perovskites $Ca/LaCu_3Fe_2Re_2O_{12}$ [8,10] and $CaCu_3Fe_2Os_2O_{12}$ [12], we can conclude that the FiM Dy^{3+}(↑)Cu^{2+}(↑)-Fe^{3+}(↑)-$Re^{4.5+}$(↓) spin alignment is formed in DCFRO at H = 6 T. Moreover, the XMCD sum rules [27,28] enable the spin and orbital moments of Cu^{2+}, Fe^{3+}, and Dy^{3+} to be calculated precisely (see Supplementary **Tab. S2** for details). Specifically, the calculated total moments are 0.63 μ_B (spin part: 0.49 μ_B) per Cu^{2+}, 4.16 μ_B (spin part: 3.94 μ_B) per Fe^{3+}, and 3.72 μ_B (spin part: 1.60 μ_B) per Dy^{3+}. If the calculated moment -1.0 μ_B (spin part: -1.36 μ_B) per $Re^{4.5+}$ of the isostructural material $LaCu_3Fe_2Re_2O_{12}$ [8] is accounted for DCFRO, then the calculated total magnetic moment of DCFRO is approximately 11.90 μ_B/f.u., close to the magnetization value measured at 2 K and 7 T (14.0 μ_B/f.u.).

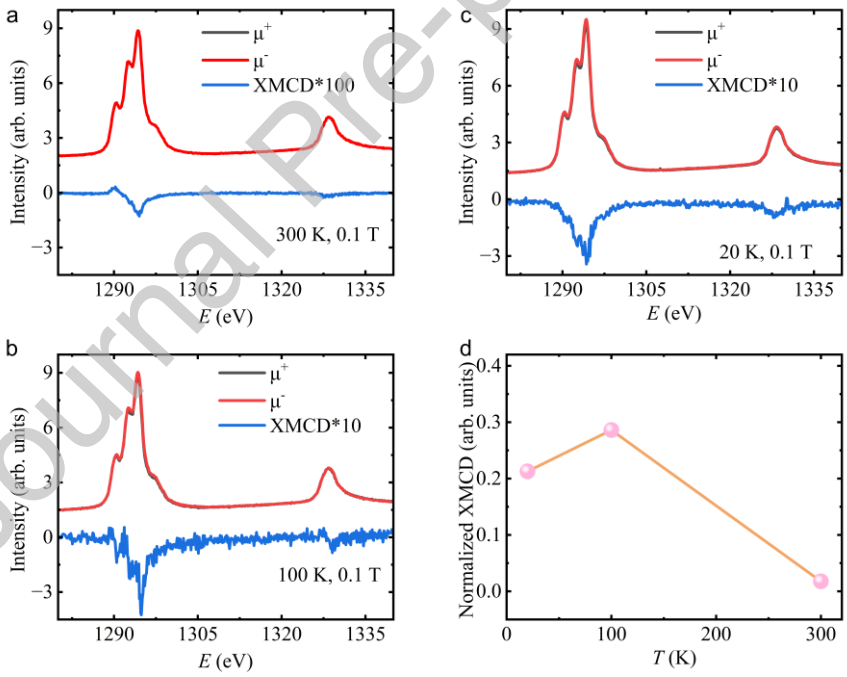

Fig. 4. (a) 300 K, (b) 100 K and (c) 20 K XMCD at the Dy-$M_{4,5}$ edges and (d) the normalized XMCD intensity of the Dy-$M_{4,5}$ edges at 300 K, 100 K and 20 K under a magnetic field of 0.01 T. Here, the normalized XMCD intensity is defined as 2*(XMCD)/(XAS^+ + XAS^-), where XAS^+ and XAS^- refer to the maximum raw XAS intensity subtracted by the background below the peak when the photon spin aligning parallel and antiparallel to the applied magnetic field, respectively.

Considering the magnetic structure of some isostructural perovskites with nonmagnetic ions at the *A*-site [8,10-12,29], the low-temperature AFM ordering of

DCFRO is likely related to Dy^{3+}. To gain deeper insight into the AFM transition of the Dy^{3+} sublattice, we measured the Dy-$M_{4,5}$ XMCD at selected temperatures by applying a weak magnetic field (0.1 T, to prevent Dy^{3+} from undergoing magnetic-field-induced spin reorientation). As shown in **Fig. 4**a-c, above 100 K, the Dy-$M_{4,5}$ XMCD signal intensifies upon cooling; however, below 100 K, such as at 20 K, the intensity drastically decreases. This behavior is more clearly evident from **Fig. 4**d, which indicates that the net magnetic moment of Dy^{3+} first increases and then decreases with decreasing temperature, thereby providing solid evidence that an AFM transition emerges in the Dy sublattice at low temperatures. The coexistence of ferromagnetism and antiferromagnetism is somewhat unusual for half metals, and the possible interplay between Dy spins and metallic electrons, as well as between the Fe and Re spin subsystems, requires further investigation. In this connection, an analogy with colossal magnetoresistivity manganites like $La_{1-x}Sr_xMnO_3$, where magnetic phase separation into ferromagnetic and antiferromagnetic phases occurs [30,31], could be useful.

3.5. Electrical and heat properties

Fig. 5a shows the temperature-dependent resistivity of DCFRO. At 0 T, the resistivity reaches 0.13 Ω cm at 300 K, and increases slightly to 0.72 Ω cm as the temperature decreases to 2 K. In contrast, at 7 T, the resistivity decreases significantly. **Fig. 5**b depicts the field-dependent magnetoresistance [MR = 100% × (ρ (H) - ρ (0))/ρ (0)] measured at 2, 50, and 150 K. The MR clearly exhibits butterfly-shaped behavior, indicating spin-dependent tunneling of the spin-polarized conduction electrons through the polycrystalline grain boundaries. As shown in **Fig. 5**c, the hysteresis field of the MR (1.45 T) was considerably stronger than that of the magnetization curve measured at 2 K (0.17 T), suggesting spin-valve-type MR originating from the intergrain tunneling of the spin-polarized carriers [8,10,11,29]. The small increase in the resistivity upon cooling, as shown in **Fig. 5**a, probably originates from the grain boundary effects of the synthesized polycrystalline sample. Thus, the transport of electrons intrinsic to DCFRO is expected to be metal-like, as confirmed by the heat capacity measurements.

As shown in **Fig. 5**d, the temperature-dependent heat capacity C_p/T exhibits an

obvious anomaly near 13 K, in agreement with the presence of Dy^{3+} spin long-range ordering around this temperature. Furthermore, the shift in the anomaly near 13 K to lower temperatures as the magnetic field becomes stronger suggests that this magnetic order is antiferromagnetic, which is in good agreement with the magnetization and XMCD results.

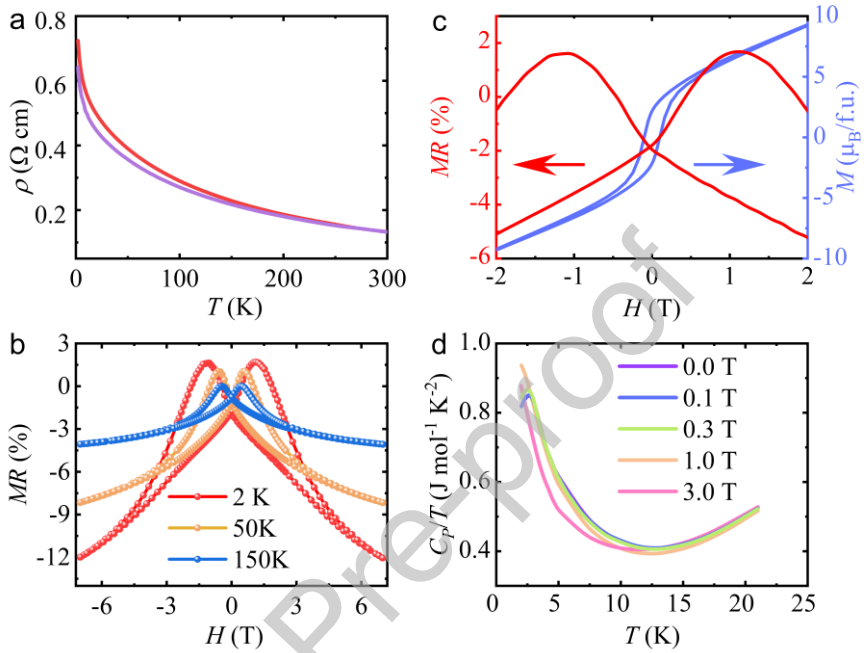

Fig. 5. (a) Temperature dependence of resistivity measured at 0 T and 7 T. (b) Field dependence of isothermal magnetoresistance between -7 and 7 T at 2 K, 50 K and 150 K. (c) Comparison of field dependence of isothermal magnetoresistance and magnetization curves measured at 2 K. (d) Temperature dependence of C_p/T measured at some selected magnetic fields.

3.6. Electronic structure

Based on the aforementioned results, it now becomes possible to discuss the electronic structure of DCFRO. The corresponding density of states (DOS) plots are presented in **Fig. 6**. The strong on-site Hubbard repulsion for the *f*-states of any rare-earth element (of the order of 7–10 eV) pushes them away from the Fermi level (E_F). This is exactly what we see in **Fig. 6**, where the occupied Dy 4*f* states appear at –8 and –10 eV, whereas the unoccupied states are at ~ 0.5 eV and 2.5 eV. Next, the same Hubbard *U* readily moves the Cu 3*d* states away from the Fermi level because the degeneracy of the e_g orbitals is lifted for square-coordinated Cu^{2+}. The Fe 3*d* states experience not only pure Hubbard repulsion but for the half-filled 3*d* shell of Fe^{3+} the intra-atomic Hund's coupling is extremely efficient; thus, the Fe orbitals are shifted

away from the Fermi level. Finally, the only orbitals in the system that remain exactly at E_F are the Re 5*d* orbitals (although they are hybridized with the other orbitals, as seen from **Fig. 6**), suggesting a half-metallic nature with an approximately 2.0 eV energy gap in the majority bands. Such a wide gap can suppress the spin-flip transitions caused by thermal excitation of the carriers, thus maintaining the half metallicity even at/above RT. Hund's intra-atomic coupling polarizes these states (the spin majority t_{2g} DOS is centered at –0.5 eV; the spin minority bands are at ~1 eV), while the superexchange interaction between the half-filled Fe and Re orbitals results in the antiferromagnetic ordering of their magnetic moments (the Cu-Re exchange interaction is also substantial, as discussed below), see [32] or [33]. Because the Fe and Re ions alternate in the quadruple perovskite lattice, the Re moments are ferromagnetically ordered. Therefore, if the effective Hubbard repulsion *U* is less than or comparable to the 4*d*/5*d* transition metal bandwidth, we inevitably encounter a half-metallic situation. One of the factors that can counteract half-metallicity is spin-orbit coupling, which mixes different spin projections. However, direct GGA+U+SOC calculations show that the spin polarization exceeds 98%.

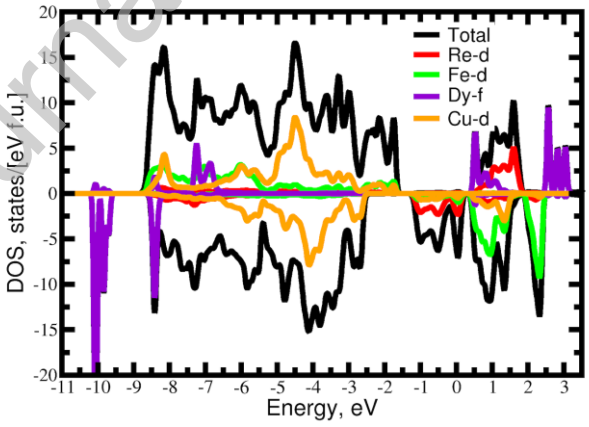

Fig. 6. Total and partial densities of states (DOS) as obtained in the GGA+U+SOC calculations. The Fermi level is set to zero.

On the other hand, the ground magnetic state in the GGA+U+SOC calculations corresponds to the situation in which the total spin moment is close to 8.0 μ_B/f.u. with the spins on Dy aligned antiparallel to each other (the spin moment of Dy inside the

Wigner-Seitz sphere is $m_s = \pm 5.0\ \mu_B$). In addition, the spin moments of Fe ($m_s = 4.1\ \mu_B$) and Re ($m_s = -1.5\ \mu_B$) are antiferromagnetically ordered and all Cu ions have the same spin projection ($m_s = 0.5\ \mu_B$). Note that the sum of the spin moments presented above deviates from 8.0 μ_B/f.u. because of the typical spin-density partitioning (over atomic spheres) problem.

Although the total spin moment per formula unit must have an integer value in half metals (because the gap for the spin minority fixes the number of electrons in both spin channels as an integer), the orbital moment for Dy and Re also make fairly large contributions. For an isolated Dy^{3+} ion with $S = 5/2$, $L = 5$, $J = 15/2$ and $g_j = 4/3$, the total magnetic moment is expected to be $m = 10\ \mu_B$. In our case, Dy^{3+} is surrounded by an O icosahedron (point group *T*), and the orbital moment could be partially quenched. Indeed, in our calculations the orbital contribution was found to be $m_l \sim 3.6\ \mu_B$ and the total magnetic moment on Dy equals 8.6 μ_B. The heavy Re ions also acquire orbital moments, but, they are much smaller than those of rare-earth ions, $m_l \sim 0.1\ \mu_B$. Thus, considering the antiferromagnetic order of the Dy moments, the total magnetization is expected to be $m_{tot} \sim 7.8\ \mu_B$/f.u. The Dy moment flips in a strong magnetic field, resulting in a total magnetic moment m_{tot} of approximately 16.3 μ_B/f.u. This overestimates the experimental value of 14 μ_B/f.u. at $H = 7$ T, and it is worth mentioning that the experimental *M*(H) does not saturate even at 7 T. It is also worth noting that, in calculations, the Fe moments form a noncollinear magnetic structure that is tilted by ~ 4° with respect to the *c*-axis, whereas the Re moments are aligned exactly along this axis. The direction of the canting coincides with the tilting of the corresponding FeO_6 octahedra (which is much larger at ~ 20°); thus, it is likely related to following the local *z*-axis of these octahedra.

To quantify the strength of the exchange interaction, Green's function method was applied to the GGA+U Hamiltonian, including the Cu-*d*, Fe-*d*, Re-*d*, and O-*p* states [34]. Analysis of the occupation matrixes and magnetic moments mentioned above shows that the valence of Fe is 3+ and therefore $S = 5/2$, that of Cu is 2+ with $S = 1/2$, while $Re^{4.5+}$ should have 2.5 electrons in the 5*d* shell, but we consider it as an *S*

= 1 ion (although strictly speaking it must be "S = 1.25") for modeling its magnetic properties by the Heisenberg model written as $H = \sum_{i>j} J_{ij} S_i S_{ij}$. Two strong antiferromagnetic exchange parameters exist between the nearest-neighbor Cu–Re and Fe-Re ions: $J_{\text{Cu-Re}}$ = 530 K and $J_{\text{Fe-Re}}$ = 84 K. The exchange fields produced by these two parameters are comparable because S_{Fe} = 5/2. The mechanism responsible for the antiferromagnetic interaction is most likely superexchange. The exchange between Fe and Cu is smaller and eventually proved to be $J_{\text{Fe-Cu}}$ = 27 K, which frustrates the system because Fe, Re, and Cu form a body-centered cubic (bcc) lattice. Here, the 5*d* shell of Re is more extended than 3*d* shells of Cu and Fe, which has stronger hybridization with O-2*p* orbitals, and has smaller Coulomb energy. Therefore, the overlap of the spin couplings to Re, i.e. the Cu/Fe-Re interactions are relatively larger in $DyCu_3Fe_2Re_2O_{12}$ as derived in our numerical calculations. In contrast, the Cu and Fe are more localized and have smaller hybridization with O-2*p* orbitals, so that they are weakly coupled. Similarly, the electron orbitals of Cu-O-Re have more overlaps than that of Fe-O-Re, and thus *A*′-site Cu and *B*′-site Re have the strongest coupling. Meanwhile, our total energy GGA+U calculations show that the exchange interaction between Dy ions is $J_{\text{Dy-Dy}}$ ~ 1 K (AFM), and it is most likely that the Ruderman-Kittel-Kasuya-Yosida (RKKY) mechanism via conduction electrons is responsible for this coupling.

Simulating temperature dependence of the heat capacity by the classical Monte-Carlo simulations of the corresponding Heisenberg model we obtain T_C ~ 410 K (see Supplementary Materials **Fig. S1**), which is smaller than experimental 650 K. However, an account of the quantum renormalization factor ($S^2 \rightarrow S(S+1)$) for Cu and Fe substantially improves the situation and leads to T_C ~ 580 K.

4. Conclusions

Using high-pressure and high-temperature methods, the *A*- and *B*-site ordered quadruple perovskite $DyCu_3Fe_2Re_2O_{12}$ was synthesized at 9 GPa and 1223 K. At approximately 660 K, this material undergoes a sharp ferrimagnetic transition with a

spin alignment of Cu^{2+}(↑)-Fe^{3+}(↑)-$Re^{4.5+}$(↓). However, when tuned by A-site Dy^{3+} antiferromagnetic ordering, the susceptibility of $DyCu_3Fe_2Re_2O_{12}$ decreases continuously below 50 K, which is different from that of other isostructural materials. Furthermore, the spins of the Dy^{3+} occupying the *A*-site become ferromagnetically ordered in a strong magnetic field to significantly enhance the magnetic moment to 14 μ_B/f.u. at 2 K, 7 T (relative to the 8.0 μ_B/f.u. of $LaCu_3Fe_2Re_2O_{12}$). The butterfly-shaped magnetoresistance behavior indicates that $DyCu_3Fe_2Re_2O_{12}$ is a half metal. Theoretical calculations also suggest that $DyCu_3Fe_2Re_2O_{12}$ is a half-metallic ferrimagnet with a wide band gap of 2.0 eV ferrimagnetic spin alignment, as observed in the experiment, and that Dy has antiferromagnetic ordering. The rare combination of a high Curie temperature, wide band gap, and large magnetic moment makes $DyCu_3Fe_2Re_2O_{12}$ a promising material for future spintronic devices and further widens the way for discovering high-performance half metals. $DyCu_3Fe_2Re_2O_{12}$ provides an interesting example in which the magnetic properties of *A*- and *B*-site ordered quadruple perovskites can be adjusted by introducing magnetic ions at the *A*-site.

Acknowledgements

This work was supported by the National Key R&D Program of China (Grants No. 2021YFA1400300), the National Natural Science Foundation of China (Grants No. 12425403, 12261131499, 11934017, 11921004, 12204516, 22271309, 12304159), and the Chinese Academy of Sciences (Grants No. XDB33000000). Z.P. thanks "Quantum" project (122021000038-7) for support analysis of calculations results. Z.L. acknowledges the support from the China Postdoctoral Innovative Talent program. The research in Dresden was partially supported by the DFG through SFB 1143. The authors acknowledge the support from the Max Planck-POSTECH-Hsinchu Center for Complex Phase Materials. Financial support for the VEKMAG project and for the PM2-VEKMAG beamline was provided by the German Federal Ministry for Education and Research (BMBF 05K2010, 05K2013, 05K2016, 05K2019) and by

HZB. Theoretical DFT calculations were supported by Russian Science Foundation (grant RSF 23-42-00069). Z.L., and J. P. contributed equally to this work.

Declaration of competing interest

The authors declare no conflict of interests.

Supplementary materials

This Supporting Information file contains the refined structure parameters, orbital and spin moments of magnetic ions for $DyCu_3Fe_2Re_2O_{12}$ calculated from XMCD data by sum rules.

Reference

[1] R.A. de Groot, F.M. Mueller, P.G. Vanengen, et al., New class of materials-half-metallic ferromagnents, Phys. Rev. Lett. 50 (1983) 2024-2027.
[2] M. I. Katsnelson, V.Y. Irkhin, L. Chioncel, et al., Half-metallic ferromagnets: From band structure to many-body effects, Rev. Mod. Phys. 80 (2008) 315-378.
[3] A. Fert, Nobel Lecture: Origin, development, and future of spintronics, Rev. Mod. Phys. 80 (2008) 1517-1530.
[4] K.L. Kobayashi, T. Kimura, H. Sawada, et al., Room-temperature magnetoresistance in an oxide material with an ordered double-perovskite structure, Nature 395 (1998) 677-680.
[5] R. Wiesendanger, H.-J. Guntherodt, G. Guntherodt, et al., Observation of vacuum tunneling of spin-polarized electrons with the scanning tunneling microscope, Phys. Rev. Lett. 65 (1990) 247–250.
[6] A. Yanase, K. Siratori, Band Structure in the High Temperature Phase of Fe_3O_4, J. Phys. Soc. Jpn. 53 (1984) 312–317.
[7] I.V. Shvets, R. Wiesendanger, D. Biirgler, et al., Progress towards spin-polarized scanning tunneling microscopy, J. Appl. Phys. 71 (1992) 5489–5499.
[8] Z. Liu, S. Zhang, X. Wang, et al., Realization of a Half Metal with a Record-High Curie Temperature in Perovskite xides. Adv. Mater. 34 (2022) e2200626.
[9] J. He, M.-X. Chen, X.-Q. Chen, et al., Structural transitions and transport-half-metallic ferromagnetism in $LaMnO_3$ at elevated pressure, Phys. Rev. B 85 (2012) 195135.
[10] W.-T. Chen, M. Mizumaki, H. Seki, et al., A half-metallic A- and B-site-ordered quadruple perovskite oxide $CaCu_3Fe_2Re_2O_{12}$ with large magnetization and a high transition temperature, Nat. Comm. 5 (2014) 3909.
[11] Z. Liu, Q. Sun, X. Ye, et al., Quadruple perovskite oxide $LaCu_3Co_2Re_2O_{12}$: A ferrimagnetic half metal with nearly 100% B-site degree of order, Appl. Phys. Lett.

117 (2020) 152402.
[12] H. Deng, M. Liu, J. Dai, et al., Strong enhancement of spin ordering by A-site magnetic ions in the ferrimagnet $CaCu_3Fe_2Os_2O_{12}$, Phys. Rev. B 94 (2016) 024414.
[13] J. Sánchez-Benítez, M. J. Martínez-Lope, J. A. Alonso, Preparation at moderate pressures, crystal and magnetic structure and magnetotransport of the ferrimagnetic perovskite $CeCu_3Mn_4O_{12}$, J. Appl. Phys. 107 (2010) 103904.
[14] J. Sa´nchez-Benı´tez, J. A. Alonso, H. Falc´ on, et al., Preparation under high pressures and neutron diffraction study of new ferromagnetic $RCu_3Mn_4O_{12}$ (R = Pr, Sm, Eu, Gd, Dy, Ho, Tm, Yb) perovskites. J. Phys.: Condens. Matter 17 (2005) S3063–S3068.
[15] H.L. Feng, M. Arai, Y. Matsushita, et al., High-Temperature Ferrimagnetism Driven by Lattice Distortion in Double Perovskite Ca_2FeOsO_6, J. Am. Chem. Soc. 136 (2014) 3326.
[16] B.H. Toby, R.B. Von Dreele, GSAS-II: the genesis of a modern open-source all purpose crystallography software package, J. Appl. Crystallogr. 46 (2013) 544-549.
[17] T. Noll, F. Radu, The mechanics of the VEKMAG experiment. Proceedings of the 9th mechanical engineering design of synchrotron radiation equipment and instrumentation conference (MEDSI2016), Barcelona, Spain, (JACoW, Geneva, 2017), (2016) 370–373.
[18] J.P. Perdew, K. Burke, M. Ernzerhof. Generalized Gradient Approximation Made Simple, Phys. Rev. Lett. (1996) 77, 3865.
[19] S.L. Dudarev, G.A. Botton, S.Y. Savrasov, et al., Electron-energy-loss spectra and the structural stability of nickel oxide: An LSDA+U study, Phys. Rev. B 57 (1998) 1505.
[20] Z.V. Pchelkina, S.V. Streltsov, Ab initio investigation of the exchange interactions in $Bi_2Fe_4O_9$: The Cairo pentagonal lattice compound, Phys. Rev. B 88 (2013) 054424.
[21] G. Kresse and J. Furthmüller. Efficient Iterative Schemes for Ab Initio Total-Energy Calculations Using a Plane-Wave Basis Set, Phys. Rev. B 54 (1996) 11169.
[22] P.E. Blöchl, Projector Augmented-Wave Method, Phys. Rev. B 50 (1994) 17953.
[23] B. Bauer, L.D. Carr, H.G. Evertz, et al., The ALPS project release 2.0: open source software for strongly correlated systems, J. Stat. Mech.: Theory Exp. (2011) P05001.
[24] M.A. Pires, C. Israel, W. Iwamoto, et al., Role of oxygen vacancies in the magnetic and dielectric properties of the high-dielectric-constant system $CaCu_3Ti_4O_{12}$: An electron-spin resonance study, Phys. Rev. B 73 (2006) 224404.
[25] Z. Liu, X. Wang, X. Ye, et al., Observation of A-site antiferromagnetic and B-site ferrimagnetic orderings in the quadruple perovskite oxide $CaCu_3Co_2Re_2O_{12}$, Phys. Rev. B 103 (2021) 014414.
[26] I. Yamada, H. Etani, K. Tsuchida, et al., Control of Bond-Strain-Induced Electronic Phase Transitions in Iron Perovskites, Inorg. Chem. 52 (2013) 13751–13761.
[27] B.T. Thole, P. Carra, F. Sette, et al., X-ray circular-dichroism as a probe of

orbital magnetization, Phys. Rev. Lett. 68 (1992) 1943-1946.
[28] P. Carra, B.T. Thole, M. Altarelli, et al., X-ray circular-dichroism and local magnetic-fields, Phys. Rev. Lett. 70 (1993) 694-697.
[29] X. Wang, M. Liu, X. Shen, et al., High-Temperature Ferrimagnetic Half Metallicity with Wide Spin-up Energy Gap in $NaCu_3Fe_2Os_2O_{12}$, Inorg. Chem. 58 (2019) 320-326.
[30] E. L Nagaev, Phys. Reports 346 (2001) 387-531.
[31] M. Yu. Kagan, K. I. Kugel, A. L. Rakhmanov, Phys. Reports 916 (2021) 1-105.
[32] D.I. Khomskii, S.V. Streltsov, Chapter in Encyclopedia of Condensed Matter Physics (2nd edition) 2 (2024) 98.
[33] J.B. Goodenough: Magnetism and the Chemical Bond, Interscience Publishers. New York, London (1963).
[34] Dm.M. Korotin, V.V. Mazurenko, V.I. Anisimov, et al., Calculation of exchange constants of the Heisenberg model in plane-wave-based methods using the Green's function approach, Phys. Rev. B 91 (2015) 224405.

Graphical Abstract

Half metals have promising applications in advanced spintronic devices because of their unique band structure. We synthesized a new high-performance half metal $DyCu_3Fe_2Re_2O_{12}$ with a high Curie temperature TC = 660 K. Moreover, at high magnetic field, the A-site Dy^{3+} spins are readily transformed into the ferromagnetic state from the antiferromagnetic ground state. The current $DyCu_3Fe_2Re_2O_{12}$ provides promising applications in advanced spintronic devices and the tuning of magnetic properties promotes an avenue for exploring high performance HMFs at room temperature

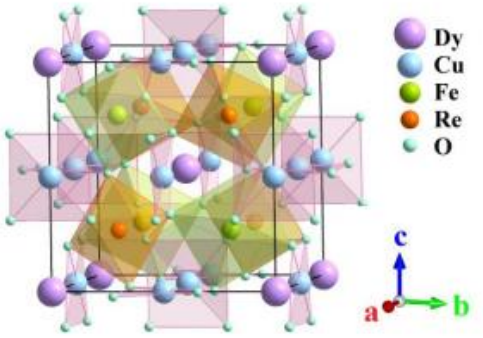

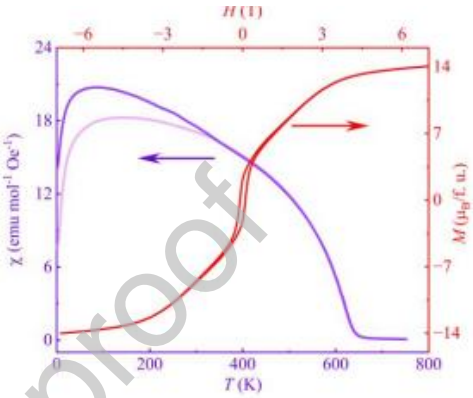

Zhehong Liu received his Ph.D. degree in 2021 at the Institute of Physics (IOP), Chinese Academy of Sciences (CAS) and engaged in postdoctoral research supported from the China Postdoctoral Innovative Talent program at IOP, CAS (2021-2023) and RIKEN (2023-now) in Japan. His research interests mainly include high-pressure synthesis and Floating Zone single crystal growth and its physical properties of novel functional materials on transition metal oxides, especially for high temperature half metals and multiferroic materials.

Peng Jinfeng received his master's degree in integrated circuits from Ningbo University in 2024. He was trained jointly by the Institute of Physics, Chinese Academy of Sciences, and now works as an electronic engineer in AAC Technologies.

Sergey V. Streltsov graduated from Ural Federal University, Russia in 2003. He obtained his Ph.D. degree in 2005 and then his doctoral degree in condensed matter physics in 2015 at the Institute of Metal Physics, Russia. In 2016 he was elected as a professor and in 2019 as a Corresponding Member of the Russian Academy of Sciences. He is the head of the Theory of Low- dimensional Spin Systems laboratory at the Institute of Metal Physics. His research interests encompass a range of topics in condensed matter physics, with an emphasis on theoretical study of the interplay among orbital, charge, spin, and lattice degrees of freedom and computational methods for application to solid-state physics.

Youwen Long (BRID: 03065.00.62665) is a Professor at the Institute of Physics, Chinese Academy of Sciences. He received his PhD degree at this institute in 2007 and engaged in postdoctoral research at Kyoto University (2007-2009) and RIKEN (2009-2011) in Japan. His major research interests include high-pressure synthesis, ambient- and high-pressure physical properties, structure–property relationships and electronic states under external stimuli for new quantum functional materials with strong electronic correlation, especially for multiferroic materials, high temperature half metals and ferromagnetic insulators and semiconductors.

Declaration of Interests

☒ The authors declare that they have no known competing financial interests or personal relationships that could have appeared to influence the work reported in this paper.

☐ The author is an Editorial Board Member/Editor-in-Chief/Associate Editor/Guest Editor for *[Journal name]* and was not involved in the editorial review or the decision to publish this article.

☐ The authors declare the following financial interests/personal relationships which may be considered as potential competing interests: